DIGITAL ACCESS TO SCHOLARSHIP AT HARVARD

Geodetic Constraints on San Francisco Bay Area Fault Slip Rates and Potential Seismogenic Asperities on the Partially Creeping Hayward Fault

(Article begins on next page)

Geodetic constraints on San Francisco Bay Area fault slip rates and potential seismogenic asperities on the partially creeping Hayward fault

Eileen L. Evans,[1] John P. Loveless,[1,2] and Brendan J. Meade[1]

[1] The Hayward fault in the San Francisco Bay Area (SFBA) is sometimes considered unusual among continental faults for exhibiting significant aseismic creep during the interseismic phase of the seismic cycle while also generating sufficient elastic strain to produce major earthquakes. Imaging the spatial variation in interseismic fault creep on the Hayward fault is complicated because of the interseismic strain accumulation associated with nearby faults in the SFBA, where the relative motion between the Pacific plate and the Sierra block is partitioned across closely spaced subparallel faults. To estimate spatially variable creep on the Hayward fault, we interpret geodetic observations with a three-dimensional kinematically consistent block model of the SFBA fault system. Resolution tests reveal that creep rate variations with a length scale of <15 km are poorly resolved below 7 km depth. In addition, creep at depth may be sensitive to assumptions about the kinematic consistency of fault slip rate models. Differential microplate motions result in a slip rate of 6.7 ± 0.8 mm/yr on the Hayward fault, and we image along-strike variations in slip deficit rate at ~15 km length scales shallower than 7 km depth. Similar to previous studies, we identify a strongly coupled asperity with a slip deficit rate of up to 4 mm/yr on the central Hayward fault that is spatially correlated with the mapped surface trace of the 1868 M_W = 6.9–7.0 Hayward earthquake and adjacent to gabbroic fault surfaces.

1. Introduction

[2] In the San Francisco Bay Area (SFBA), motion between the Pacific plate and Sierra Block is partitioned across 7 major subparallel right-lateral faults with <20 km spacing [e.g., *Freymueller et al.*, 1999]. From west to east, these include the San Gregorio, San Andreas, Hayward, Rodgers Creek, Calaveras, Green Valley, and the Greenville faults (Figure 1). The Hayward fault lies in the center of the SFBA fault system accommodating ~20% of the total slip budget [e.g., *Graymer et al.*, 2002; *Schmidt et al.*, 2005; *d'Alessio et al.*, 2005], and has been interpreted as the SFBA fault most likely to rupture in a M_W = 6.7 or larger earthquake in the next 20 years [*2007 Working Group for California Earthquake Probabilities*, 2008] based on paleoseismic estimates of earthquake recurrence intervals and geologic and geodetic fault slip rate estimates. The last major (M_W = 7) Hayward fault earthquake occurred in 1868,

with a reported surface rupture from Fremont in the south to San Leandro in the north (Figure 1) [*Lawson*, 1908; *Yu and Segall*, 1996; *Bakun*, 1999; *Toppozada and Branum*, 2004].

[3] The Hayward fault is both geometrically [*Graymer et al.*, 2005; *Waldhauser and Ellsworth*, 2002; *Hardebeck et al.*, 2007] and kinematically complex [*Lienkaemper et al.* 2001; *Simpson et al.*, 2001; *Schmidt et al.*, 2005; G. J. Funning et al., The source of major earthquakes on the Hayward fault, California, submitted to *Geophysical Research Letters*, 2011]. Nearly vertical along most of its trace, the Hayward fault dips eastward south of Fremont, as illuminated by relocated seismicity [*Waldhauser and Ellsworth*, 2002; *Manaker et al.*, 2005; *Hardebeck et al.*, 2007], and likely merges at depth with the Calaveras fault immediately to the east [*Ponce et al.*, 2004; *Williams et al.*, 2005; *Graymer et al.*, 2005]. Surface creep observations from creepmeters [*Bilham and Whitehead*, 1997] and alignment arrays [*Lienkaemper et al.*, 2001; *Simpson et al.*, 2001] show that sections of the Hayward fault creep aseismically with surface creep rates ranging from <4 mm/yr on the northern Hayward fault to 8 mm/yr near Fremont. Estimates of spatially variable creep on the Hayward fault from inversions of GPS and InSAR data [*Bürgmann et al.*, 2000; *Schmidt et al.*, 2005; Funning et al., submitted manuscript, 2011] suggest that the distribution of interseismic

---

[1]Department of Earth and Planetary Sciences, Harvard University, Cambridge, Massachusetts, USA.
[2]Now at Department of Geosciences, Smith College, Northampton, Massachusetts, USA.
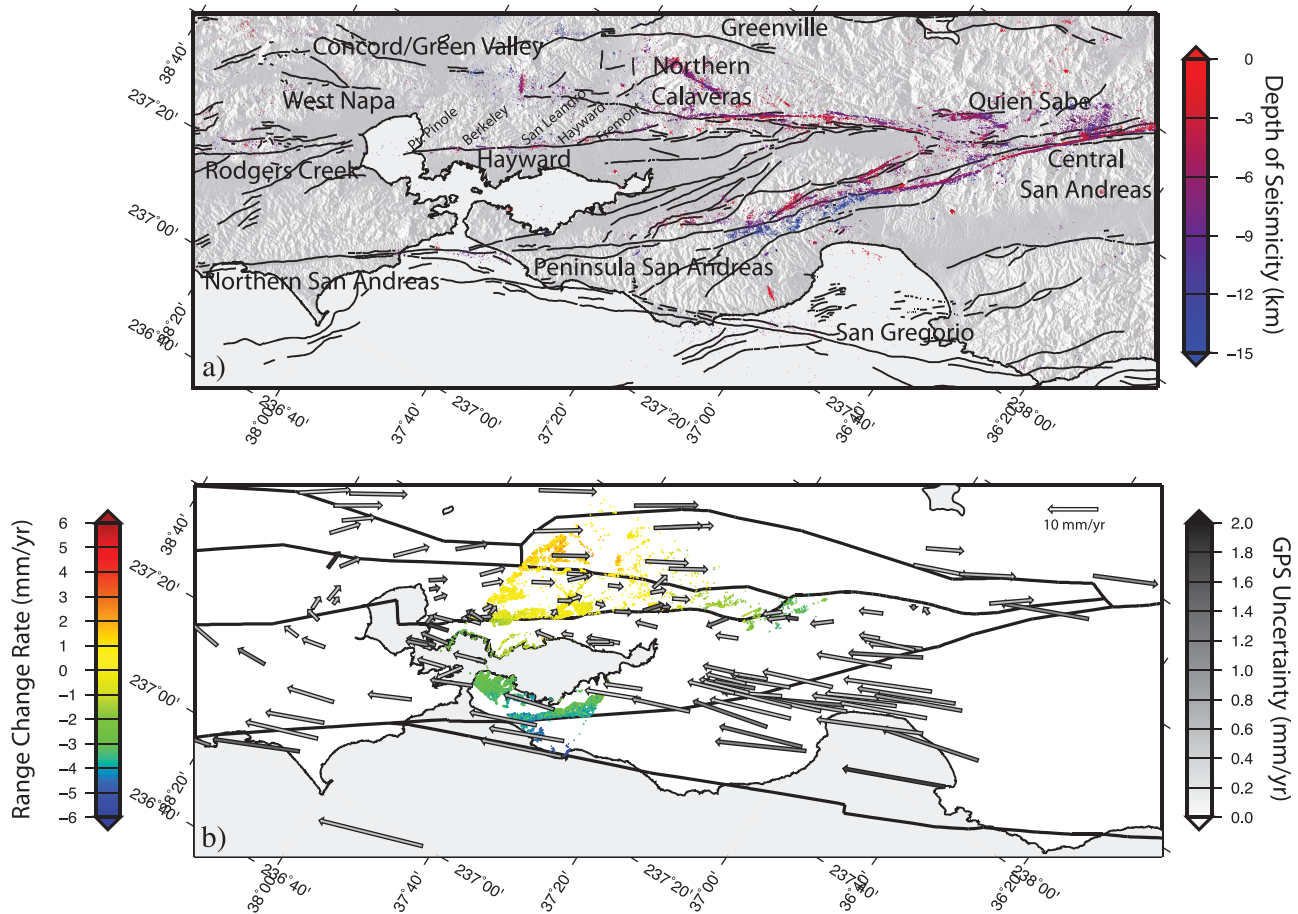
Figure 1. (a) San Francisco topography and mapped fault locations; seismicity [*Waldhauser and Ellsworth*, 2002] shown colored by depth of hypocenter. (b) Block boundaries based on mapped fault locations shown as bold black lines. Bay Area GPS velocities (BAVU) shown as vectors colored by uncertainty. Filtered InSAR range change rates from *Bürgmann et al.* [2006].

fault coupling is also spatially heterogeneous, ranging from 0 to 8 mm/yr over <15 km length scales both along strike and downdip. Dynamically driven models [e.g., *Savage and Lisowski*, 1993; *Simpson et al.*, 2001, *Malservisi et al.*, 2003] of creep on the Hayward fault have been interpreted to agree favorably with geodetically inferred estimates of creep at depth.

[4] Imaging the interseismic creep on the Hayward fault is complicated because the geodetic observations that provide the greatest resolution of activity at depth [*Schmidt et al.*, 2005] are also influenced by the overlapping interseismic elastic strain fields associated with each of the closely spaced faults of the SFBA fault system [e.g., *Freymueller et al.*, 1999]. Thus, to some extent, estimates of Hayward fault creep at depth depend on assumptions about the behavior of the rest of the SFBA fault system. Previous geodetically constrained kinematic models of Hayward fault behavior may be categorized into three classes: (1) those that incorporate spatially dense InSAR measurements near the Hayward fault but do not assume that slip rates are kinematically consistent [*Schmidt et al.*, 2005; Funning et al., submitted manuscript, 2011], (2) those that assume SFBA

fault slip rates are kinematically consistent but do not include spatially dense InSAR measurements near the Hayward fault [*Murray and Segall*, 2001; *d'Alessio et al.*, 2005; *Johnson and Fukuda*, 2010], and (3) those that both assume SFBA fault flip rates are kinematically consistent and include InSAR measurements [*Bürgmann et al.*, 2000].

[5] Here we develop a kinematically consistent three-dimensional block model of the SFBA fault system constrained by both GPS and spatially dense InSAR observations that provide the greatest resolution of fault activity at depth. We simultaneously estimate microplate rotations, kinematically consistent fault slip rates, and spatially variable slip deficit at depth on the Hayward fault. This particular reference model is not constrained by a priori geologic slip rate constraints or surface creep measurements, so that the model may be tested against these observations. We perform checkerboard resolution tests on the Hayward fault within the three-dimensional SFBA block model to assess the resolving ability of the data and determine the extent to which creeping behavior can be imaged at depth. To understand how the assumption of kinematically consistent slip rates affects Hayward fault creep rate estimates, we

develop a series of idealized two-fault deep dislocation models that may explain differences between this and some previous studies.

2. Interseismic Deformation in Fault Systems

[6] Interseismic deformation in fault systems such as the SFBA includes the contribution of earthquake cycle processes associated with multiple faults. The quasistatic earthquake cycle contribution from SFBA faults has been approximated with deep dislocation [*Bürgmann et al.*, 2000; *Schmidt et al.*, 2005; Funning et al., submitted manuscript, 2011], and block models [*Murray and Segall*, 2001; *d'Alessio et al.*, 2005; *Johnson and Fukuda*, 2010]. In the deep dislocation formulation, the net surface velocity field resulting from a partially creeping fault such as the Hayward is described as the sum of the deep dislocation and creep contributions $v_{net} = v_{deep} + v_{creep}$. Partial creep refers to aseismic fault creep at rates at or below the long-term slip rate.

[7] In this study, we estimate partial creep on the Hayward fault in terms of slip deficit within a kinematically consistent block model of the SFBA fault system, assuming steady state interseismic behavior, similar to previous studies of subduction zone environments [e.g., *Wallace et al.*, 2004; *Bürgmann et al.*, 2005; *Loveless and Meade*, 2010; *McCaffrey*, 2009]. In the block model formulation, the upper crust is divided into microplates bounded by faults, and fault slip rates are linearly proportional to the differential rotation rates at block boundaries, so that slip rates are implicitly kinematically consistent [*Matsu'ura et al.*, 1986; *Bennett et al.*, 1996; *Souter*, 1998; *McCaffrey*, 2002; *Meade and Hager*, 2005; *Meade and Loveless*, 2009]. Kinematic consistency is defined such that a path integral of motion (slip rates and plate rotations) across the plate boundary sums to the total relative tectonic plate motion, independent of path [*Minster and Jordan*, 1978; *Humphreys and Weldon*, 1994]. Interseismic fault slip rates are determined by the rotation rate of adjacent microplates [*Souter*, 1998], and the elastic contribution to the surface velocity field depends on the degree of slip deficit along these faults [*Meade and Hager*, 2005]. In this formulation, the resulting velocity field due to a partially creeping fault is equal to the contribution from the total static block offset minus the contribution to the velocity field due to the elastic slip deficit, $v_{net} = v_{block} - v_{slip\ deficit}$. Estimates of interseismic creep and slip deficit rates map into the other as $\dot{s}_{creep} = \dot{s}_{long\ term} - \dot{s}_{slip\ deficit}$. We determine creep rates on the Hayward fault from directly estimated slip deficit rates. The particular linear block model formulation used here [*Meade and Loveless*, 2009] is similar to that used in other SFBA studies [*Matsu'ura et al.*, 1986; *Murray and Segall*, 2001; *d'Alessio et al.*, 2005] with the addition of spatially variable fault coupling on the Hayward fault, and without geologic fault slip rate assumptions [*Johnson and Fukuda*, 2010].

3. Geodetic Observations and Reference Block Model Geometry

[8] For this study we modify the block model formulation [*Meade and Loveless*, 2009] to include InSAR observations (Appendix A). The geodetic data that we consider are 191 nominally interseismic GPS velocities and 15,000 PS-InSAR (Permanent Scatterer) line-of-sight range change rates collected from 1992 to 2000 by the European Remote Sensing satellites ERS-1 and ERS-2 [*Bürgmann et al.*, 2006] (Figure 1). Survey mode GPS velocities in the SFBA are those reported by *d'Alessio et al.* [2005], augmented by 6 GPS velocities at sites in the Pacific (sites KWJ1, CHAT, KOKB, MKEA, THTI, MAUI) and 9 in eastern North America (sites WES2, BARN, THU1, THU3, SCH2, BRMU, ALRT, STJO, KELY) to constrain far-field plate motions. Because this study is focused on understanding steady interseismic fault system behavior, we do not include velocities from GPS stations that have documented postseismic deformation following the M_W = 6.9–7.0 1989 Loma Prieta Earthquake [*Bürgmann et al.*, 1997]. The InSAR data [*Bürgmann et al.*, 2006] are filtered to remove observations that may be affected by seasonal groundwater effects and local spatially incoherent motions by removing all observations on Quaternary units, and retaining only range change rates of greater than −10 mm/yr and less than 10 mm/yr. We additionally remove observations differing from the mean of all stations within 5 km by more than 1 mm/yr. The resulting filtered InSAR observations were then cropped to remove observations in the Santa Cruz mountains and the Southern Calaveras fault (Figure 1) that may be biased by ongoing postseismic deformation from the Loma Prieta Earthquake. The final InSAR data set retains the 15,000 most coherent observations. There are 7,144 observations within 5 km of either side of the Hayward fault, although data density decreases toward the south because of the presence of Quaternary units and vegetation. Within the block model formulation, we account for uncertainties in satellite orbits by simultaneously estimating a best fitting quadratic ramp [e.g., *Pritchard et al.*, 2002, *Zebker et al.*, 1994] (Appendix A).

[9] The block geometry for a reference SFBA model is informed by mapped active faults [*Graymer et al.*, 2002] and previous regional crustal deformation studies (Figure 1). We use a reference block model geometry that is similar to *d'Alessio et al.* [2005]. Our SFBA plate boundary block model is divided into six blocks between the Pacific block to the west and the Sierra Nevada block to the east (Figure 2). The San Francisco peninsula block is separated from the Pacific block by the San Gregorio fault and bounded by the San Andreas fault in the east. East of the San Andreas fault is the Bay block, bordered on the east by the Rodgers Creek, Hayward, and Calaveras faults. The East Bay block lies between the Hayward and Rodgers Creek faults to the west and the Northern Calaveras fault to the east. The northeast SFBA contains the Napa Block, bounded by the West Napa fault in the west and the Green Valley and Concord faults in the east. The Greenville fault separates the East Bay Hills block from the Sierra Nevada block, which bounds the entire SFBA fault system to the east. To complete the plate boundary, we include a coarse representation of the North America block east of the Sierra Nevada block.

[10] The most notable geometric difference between this reference block model and previous models [*d'Alessio et al.*, 2005; *Johnson and Fukuda*, 2010] is that we do not include the Great Valley fault as a structure subparallel to the SAF. Instead, we hypothesize that the Greenville fault in the east SFBA transfers slip to the Quien Sabe fault (Figure 1).
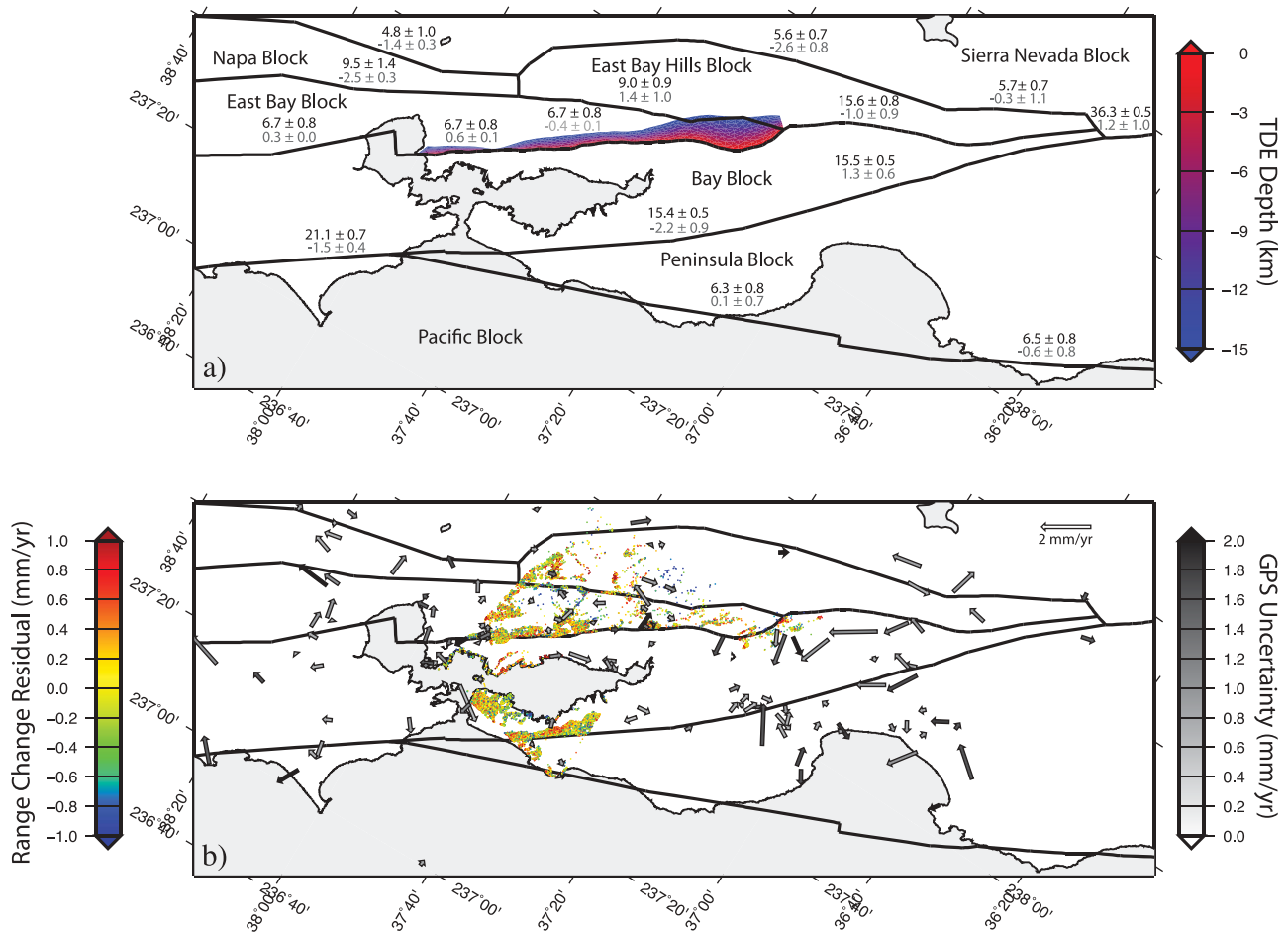
Figure 2. (a) Block geometry with labeled blocks. On-fault estimated strike-slip rates are shown in black and dip-slip rates are shown in gray. Negative dip-slip rate is tensile. Mesh of triangular dislocation elements used to estimate spatially variable coupling colored by depth of element. (b) Residual InSAR range change rates and GPS velocities.

Repeating microearthquakes on this structure indicate that it is distinct from the neighboring southern Calaveras fault and may actively creep [*Templeton et al.*, 2008]. This difference in model geometry is consistent with the idea that all of the slip in the SFBA is fed from San Andreas and San Gregorio faults in central California and is discussed in section 4. All faults other than the Hayward fault are represented using rectangular dislocation elements [*Okada*, 1985] that are assumed to be locked from the surface to an effective locking depth during the interseismic stage of the seismic cycle. InSAR data near the trace of the Hayward fault [*Schmidt et al.*, 2005; *Bürgmann et al.*, 2006; Funning et al., submitted manuscript, 2011] are spatially dense enough to enable us to constrain spatial variations in fault coupling in this region. Although nearly vertical for most of its trace, the Hayward fault dips east south of Fremont, California, and likely merges with the Calaveras fault at depth [*Waldhauser and Ellsworth*, 2002; *Manaker et al.*, 2005; *Graymer et al.*, 2005; *Hardebeck et al.*, 2007]. The geometry of the Hayward fault is represented by a three-dimensional mesh of 1006 triangular dislocation elements [*Comninou*, 1973; *Jeyakumaran et al.*, 1992; *Thomas*, 1993; *Meade*, 2007], derived from relocated seismicity and geologic mapping

[*Murray-Moraleda and Simpson*, 2009]. We estimate spatially variable coupling on the portion of the Hayward fault north of the step over to the Calaveras fault east of San Jose. In addition to the reference model described above, we have tested block boundary geometries with and without stepovers on the Calaveras-Concord-Green Valley system and in San Pablo Bay and find negligible differences in slip rate estimates on SFBA faults.

4. Estimated Fault Slip and Creep Rates

[11] We jointly invert GPS and InSAR data for the best fitting set of block rotation vectors and fault slip rates (Appendix A). Because there are approximately two orders of magnitude more InSAR observations than GPS observations, the InSAR data as a whole have a dominant influence on the solution unless they are downweighted. In our reference model the weighting ratio of the InSAR data relative to the GPS data, β_{SAR}, is set to 0.1 so that no individual InSAR pixel has more of an influence over the solution than the GPS velocity with the smallest uncertainty (Appendix A). We also regularize the solution by smoothing the slip deficit rates on the mesh of triangular dislocation elements by
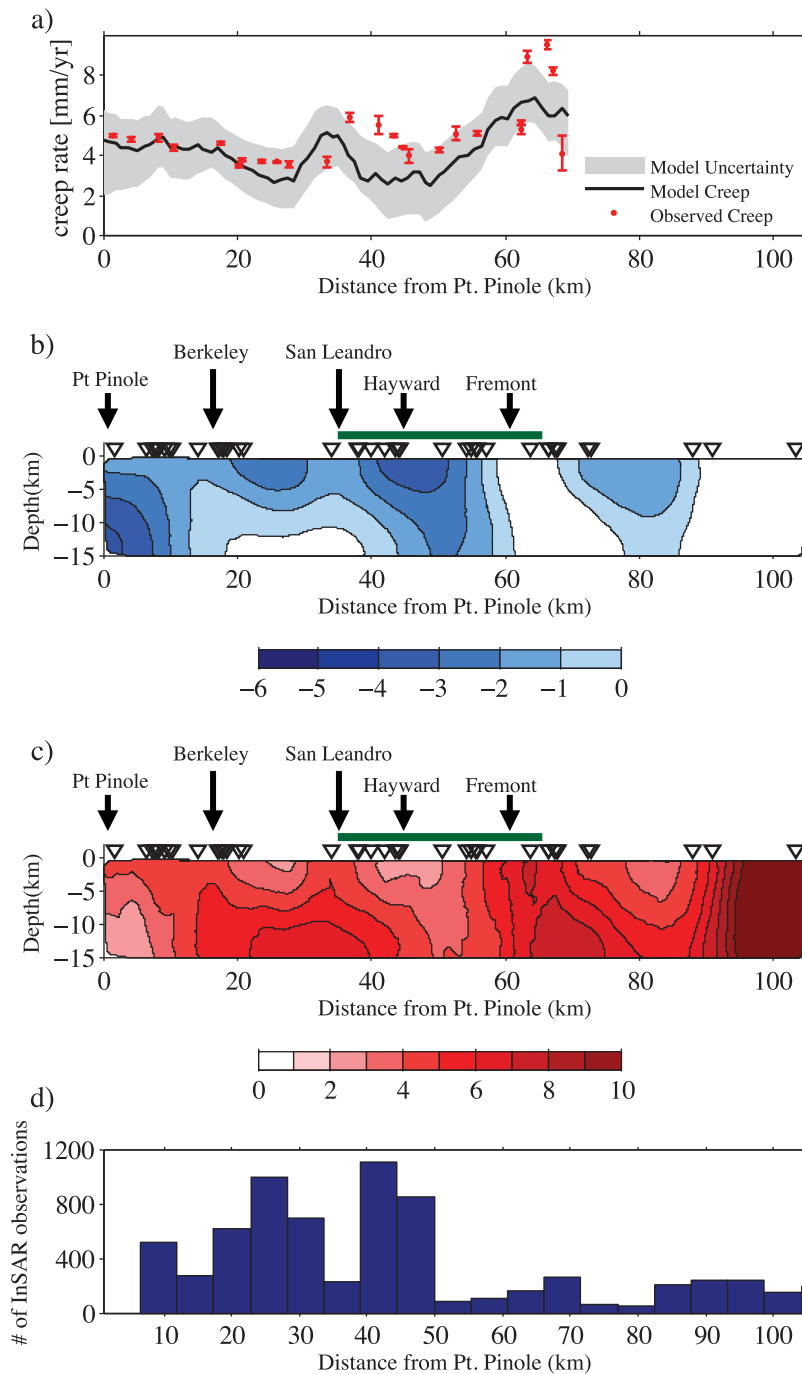
Figure 3. (a) Observed creep rates and estimated creep (estimated long-term slip-estimated coupling) on the surface triangular dislocation elements of our reference coupling distribution shown with 67% confidence bounds. (b) Reference slip deficit distribution on the Hayward fault estimated on a mesh of triangular dislocation elements. High coupling rates (dark blue) correspond to locked regions. Low slip deficit rates (white) represent creeping sections. Black triangles represent GPS station locations. Green bar represents the observed surface trace of the 1868 Hayward earthquake. (c) Reference creep distribution (estimated long-term slip minus estimated slip deficit rate) for the fault surface. (d) Histogram showing density of SAR data points within 5 km of either side of the fault.

minimizing the gradient of coupling rate between adjacent triangles [e.g., *Harris and Segall*, 1987, *Maerten et al.*, 2005]. We choose the smoothing constant, β^*, based on the resolution tests described in section 5. The reference model (Figures 2 and 3) with $\beta^* = 5$ reproduces the SFBA GPS velocity field and InSAR range change rates with a mean residual GPS velocity magnitude of 1.4 mm/yr (WRSS per station = 6.1) and mean residual InSAR range change rate of 0.4 mm/yr.
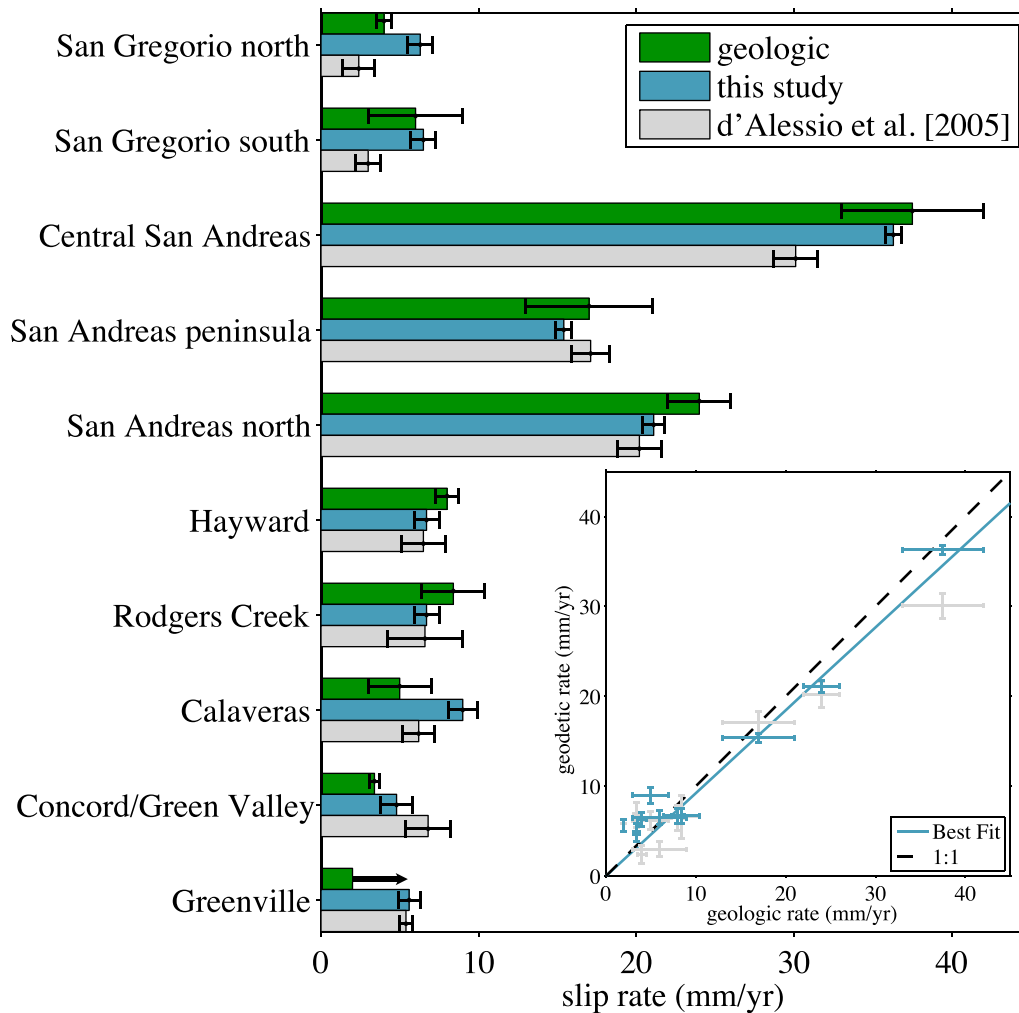
Figure 4. Slip rate comparison for this and previous SFBA studies. (inset) Comparison of geologic and geodetic rates for this study and *d'Alessio et al.* [2005], best fit line shown in blue, dashed line is 1:1. References for geologic slip rates: San Gregorio north [*Simpson et al.*, 1998], San Gregorio south [*Weber and Nolan*, 1995], central San Andreas [*Segall*, 2002], San Andreas peninsula [*Hall et al.*, 1999], San Andreas north [*Niemi and Hall*, 1992], Hayward [*Lienkaemper and Borchardt*, 1996], Rodgers Creek [*Budding et al.*, 1991], Calaveras [*Kelson et al.*, 1996], Concord [*Borchardt et al.*, 1999], Greenville [*Berger et al.*, 2010] (minimum rate).

[12] Geodetic slip rate estimates on SFBA faults from this study and *d'Alessio et al.* [2005] are compared with geologic slip rate estimates in Figure 4. Plotting geodetic slip rates against geologic slip rates, the best fit line through the origin is indistinguishable from a 1-to-1 line at the 95% confidence level (Figure 4, inset). We estimate a slip rate of 9.0 ± 0.9 mm/yr on the Calaveras fault, which is faster than both the previous geologic slip rate estimate of 5.0 ± 2 mm/yr [*Simpson et al.*, 1999] and the previous geodetic estimate of 6.2 ± 1.0 [*d'Alessio et al.*, 2005] (Figure 4). A slip rate estimate of 5.6 ± 0.7 mm/yr on the Greenville fault is consistent with a recent study estimating a minimum geologic fault slip rate of 2 mm/yr from offset sediments [*Berger et al.*, 2010] (Figure 4). A slip rate of 5.7 ± 0.7 mm/yr on the Quien Sabe fault is also consistent with estimates of 11 cm of creep offset over 22 years of observations estimated from repeating microearthquakes on the fault [*Templeton et al.*, 2008], although the use of repeating microearthquakes as

creepmeters is ambiguous [*Sammis and Rice*, 2001]. We estimate 36.3 ± 0.5 mm/yr on the central San Andreas fault south of Hollister. This is consistent with previous geodetic estimates in this region [*Johanson and Bürgmann*, 2005], and with estimates north of Parkfield, California [*Argus and Gordon*, 2001; *Segall*, 2002; *Becker et al.*, 2005, *Meade and Hager*, 2005; *Schmalzle et al.*, 2006]. This agreement supports the idea that slip transfers directly into the SFBA from the San Andreas and San Gregorio faults in central California.

[13] We estimate that the Hayward fault is fully to partially creeping along its entire length and down to at least 7 km depth (Figure 3). Although short-wavelength features (<15 km) cannot be robustly resolved below 7 km depth (see section 5), Figure 3 shows the complete slip deficit and creep rate estimates from the reference model, in which the Hayward fault extends to 15 km depth. Above 7 km, slip deficit rates appear to decrease, and creep rates increase, with depth. We estimate the long-term fault slip rate on the
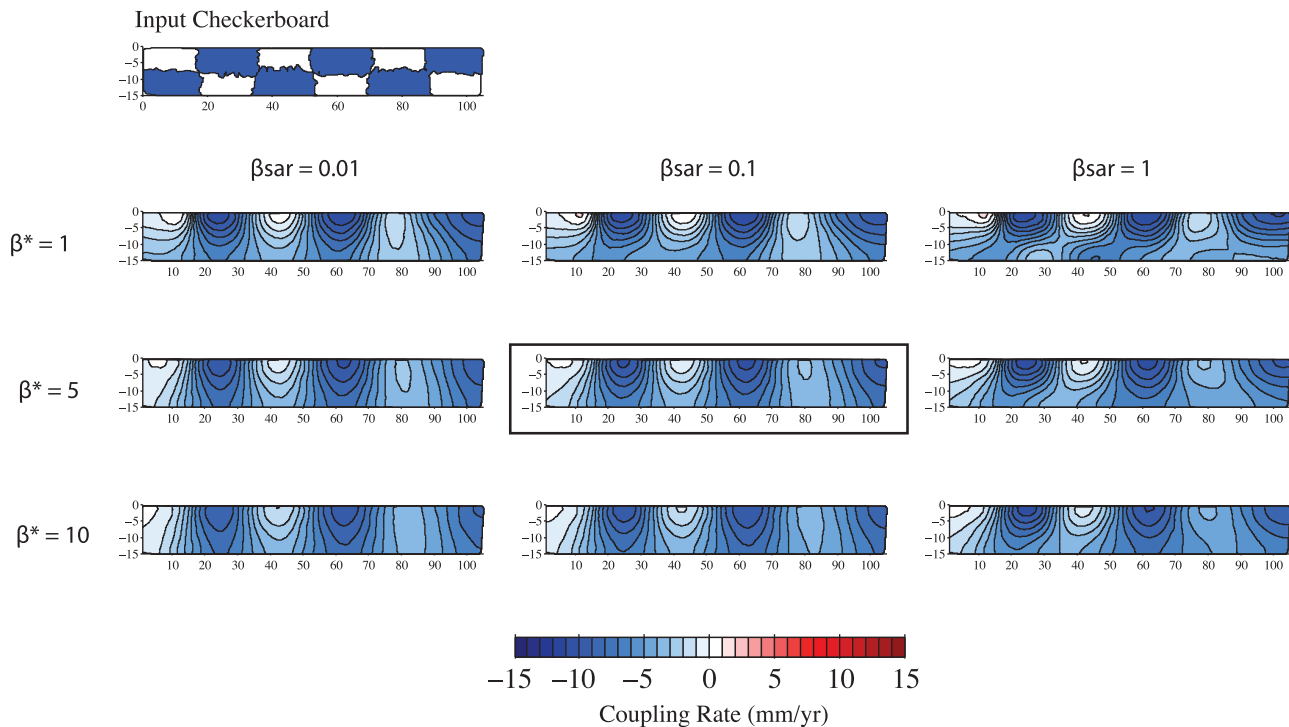
Figure 5. Checkerboard resolution tests. We assign a known coupling distribution (input checkerboard) to the Hayward fault mesh of triangular dislocation elements, generate synthetic GPS and InSAR surface observations with a forward model, and invert to recover the input coupling distribution. Contribution to the solution from InSAR relative to GPS β_{SAR} increases from left to right. The smoothing constant β^{*} increases from top to bottom. Constants corresponding to the reference model are shown with black box.

Hayward fault to be 6.7 ± 0.8 mm/yr, which is 1 to 4 mm/yr lower than previous estimates of long-term slip rates on the Hayward fault [*d'Alessio et al.*, 2005; *Lienkaemper and Borchardt*, 1996; *Graymer et al.*, 2002] (Figure 4). Similar to previous Hayward fault studies [e.g., *Simpson et al.*, 2001; *Schmidt et al.*, 2005; Funning et al., submitted manuscript, 2011], we find maximum coupling rates of 4.3 ± 1.4 mm/yr at depth beneath Point Pinole, although the lack of InSAR data at the northern end of the Hayward fault limits resolution here. High surface creep rates near Point Pinole (4.1 ± 2.1 mm/yr) and near Fremont, California (7.2 ± 1.5 mm/yr) are generally consistent with observations [*Bilham and Whitehead*, 1997; *Lienkaemper et al.*, 2001] (Figure 3a). Within 67% confidence bounds, model surface creep rate estimates and creep rate measurements agree at 19 of the 25 alignment array observation locations [*Lienkaemper et al.*, 2001]. The southern portion of the creep distribution shows a rapid increase in creep rate at the surface and at depth, supporting the hypothesis that the Hayward fault merges around 90 km from Point Pinole with the Calaveras fault to the east [*Lienkaemper and Galehouse*, 1998; *Waldhauser and Ellsworth*, 2002; *Ponce et al.*, 2004; *Williams et al.*, 2005; *Manaker et al.*, 2005; *Graymer et al.*, 2005]. A period of decreased creep on the southern Hayward fault from 1989 to 1996 following the 1989 $M_w = 7.0$ Loma Prieta earthquake [*Lienkaemper et al.*, 1997; *Lienkaemper et al.*, 2001] would be captured in the InSAR data spanning 1992–2000, and included in the slip distribution estimated here, which represents an average over this time period. However, because the density of InSAR observations within 5 km of the Hayward fault decreases north of Fremont

(Figure 3), where the decrease in creep rate was most dramatic [*Lienkaemper et al.*, 1997; *Lienkaemper et al.*, 2001], we do not expect a large affect in the creep distribution (assuming creep rate changes were not persistent at depth). Between San Leandro and Fremont, spatially coincident with the surface rupture in the 1868 Hayward earthquake [*Lawson*, 1908] and a 25 km long gabbroic body on both faces of the Hayward fault [*Graymer et al.*, 2005], we estimate a 20 km long segment with slip deficit rates of up to 3.7 ± 1.2 mm/yr at the surface (Figure 3b).

5. Hayward Fault Resolution Tests

[14] To determine how well the current distribution of GPS and InSAR observations can be used to resolve coupling on the Hayward fault in the context of the elastic block model used here, we perform a series of checkerboard resolution tests [e.g., *Bürgmann et al.*, 2005, *Loveless and Meade*, 2010]. We create a synthetic coupling distribution in a checkerboard pattern (Figure 5) in which patches of 20 km by 7.5 km are assigned coupling rates alternating between 10 mm/yr and 0 mm/yr. We run forward block models (using the same geometry as the reference model) with this known coupling distribution to generate synthetic GPS velocities and synthetic InSAR range change rates at the same observation coordinates as the real data. Inverting the synthetic geodetic data to see how well a known slip deficit distribution can be recovered provides an assessment of the resolving ability of the data at different points along
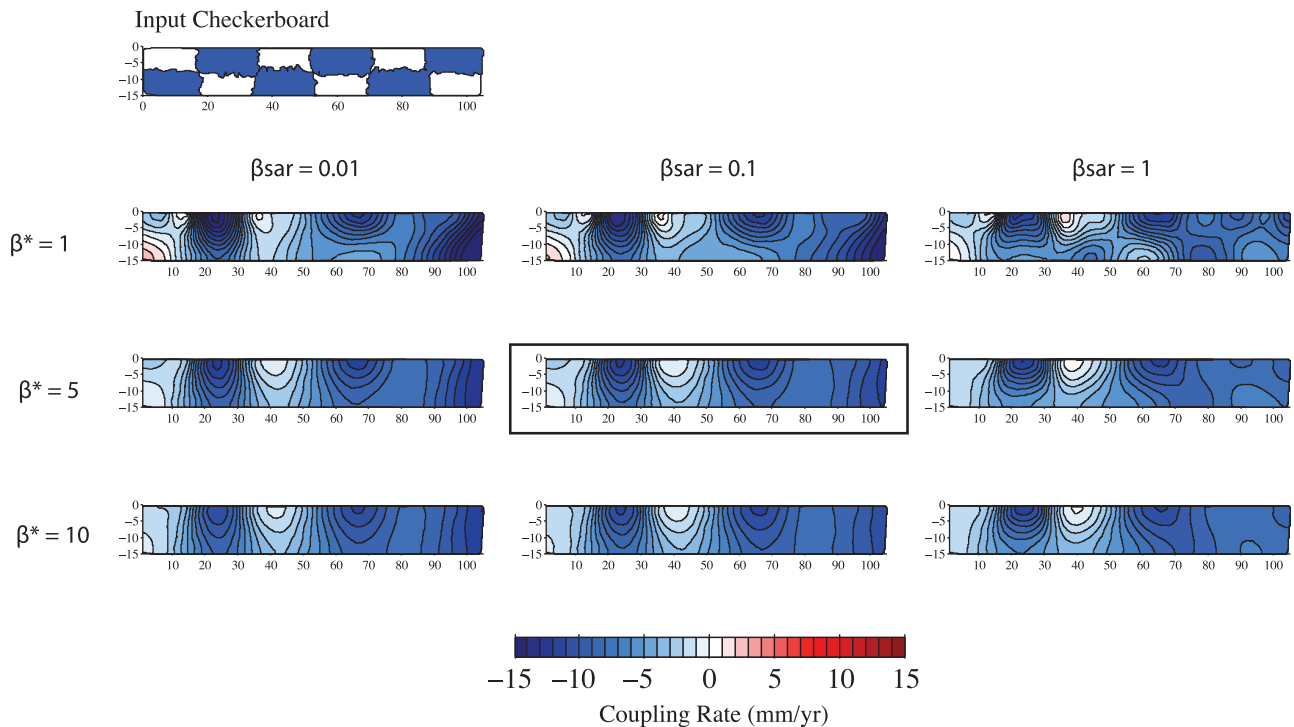
Input Checkerboard

Figure 6. Checkerboard resolution tests with noise added. Noise sampled from a normal distribution with mean of 0.5 mm/yr and added to synthetic GPS and SAR rates. We assign a known coupling distribution (input checkerboard, see Figure 5) to the Hayward fault mesh of triangular dislocation elements and generate synthetic GPS and InSAR surface observations with a forward model. We then add noise sampled from a normal distribution with mean of 1 mm/yr and invert to recover the input coupling distribution. Contribution to the solution from InSAR relative to GPS β_{SAR} increases from left to right. The smoothing constant β^* increases from top to bottom. Constants corresponding to the reference model shown with black box.

the fault and allows us to systematically test the sensitivity to variations in weighting parameters.

[15] The resolved coupling distribution varies based on the contribution to the solution of InSAR data relative to GPS data and on the degree of spatial smoothing [e.g., *Menke*, 1984]. When the ratio β_{SAR} is equal to one, every InSAR range change rate is given the same weight as each GPS velocity. Higher β_{SAR} values improve spatial resolution on the triangular dislocation elements because of the greater density of InSAR observations near the fault. Decreasing the smoothing constant β^* for a given data weight ratio sharpens the boundaries of the checkerboard pattern. Figure 5 shows the results of 9 realizations of the checkerboard resolution test with weighting ratio ranging from $\beta_{SAR} = 0.01$ to $\beta_{SAR} = 1$ and smoothing values ranging from $\beta^* = 1$ to $\beta^* = 10$. Features at ~15 km wavelength are resolvable where $\beta^* = 1$, $\beta_{SAR} = 1$ (Figure 5). At distances of 40–70 km south of Point Pinole, this resolution test overestimates coupling by ~1 mm/yr at the surface and underestimates coupling by ~2 mm/yr at 10 km depth. Farther south than 70 km, resolution at depth deteriorates such that we recover only 5 mm/yr of the input 10 mm/yr patch at depth between 70 and 90 km from Point Pinole (Figure 5).

[16] Adding noise to the synthetic velocities computed from the forward model reduces resolution of the recovered coupling distribution (Figure 6). We add noise sampled from a normal distribution with a standard deviation of 1 mm/yr to the synthetic velocities and range change rates. At low smoothing values of $\beta^* = 1$, estimated coupling rates overshoot the input coupling rates by up to 8 mm/yr. Increasing smoothing to $\beta^* = 5$ and $\beta^* = 10$ resolves coupling rates between 0 and 10 mm/yr, but cannot resolve sharp boundaries between patches. In general, estimated coupling rates still recover the checkerboard pattern on the northern part of the triangular mesh and at the surface, but lose resolution south of about 60 km from Point Pinole and below 7 km depth. Higher β_{SAR} values improve spatial resolution on the triangular dislocation elements, but higher smoothing values are required to recover coupling magnitudes similar to input values (Figure 6). We choose a smoothing value of $\beta^* = 5$ and weight ratio of $\beta_{SAR} = 0.1$ for our reference model to capture along strike coupling variations with minimal overshoot in the coupling rate estimates (Figure 3).

[17] The resolution tests demonstrate that we are able to resolve coupling features of 15–20 km in wavelength along strike, especially 10–80 km south of Point Pinole. At high smoothing weights, resolution at depth deteriorates. With an InSAR weight $\beta_{SAR} = 0.1$, and smoothing weight $\beta^* = 5$, the checkerboard resolution tests are not successful at recovering slip deficit features <15 km in length below 7 km depth.
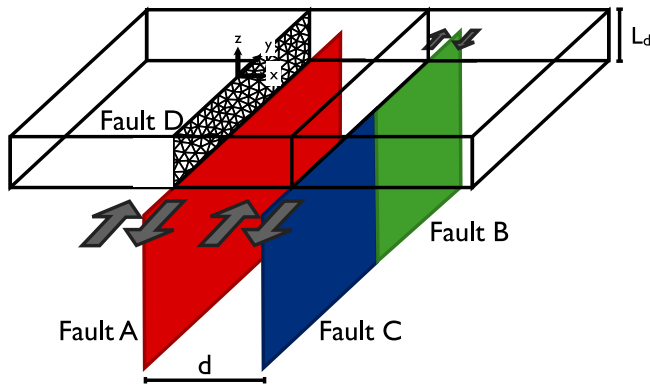
Figure 7. Simple model setup. Faults A, B, and C are very long parallel strike-slip fault segments in a homogeneous elastic half-space extending from a locking depth L_d to infinite depth and separated by distance d. Fault D is a mesh of triangular dislocation elements between the locking depth L_d and the surface and is assumed to be fully locked. When faults B and C slip at the same rate, the system is kinematically consistent. Kinematic inconsistency can be introduced by assuming an a priori slip rate on fault B that is inconsistent with fault C. Estimates of nonzero slip on fault D represent modeling artifacts.

In interpreting model results, slip deficit estimates deeper than 7 km should be considered within the context of these resolution tests.

6. Simple Models of the Effects of Kinematically Consistent and Inconsistent Fault Systems on Creep Distributions

[18] Creep rate estimates on the Hayward fault at depth suffer not only from poor resolution, but are also sensitive to model assumptions about the kinematic consistency of closely spaced SFBA faults. For example, Hayward fault creep rates at depth estimated with a kinematically consistent SFBA fault system model [*Bürgmann et al.*, 2000] differ from those derived from models with kinematically inconsistent fault slip rates [*Schmidt et al.*, 2005; Funning et al., submitted manuscript, 2011]. To understand how assumptions of kinematic consistency affect creep rate estimates, we develop a simple model consisting of a pair of very long parallel strike slip faults modeled as deep dislocations in a homogeneous elastic halfspace. Fault slip rates and geometry are assumed to be similar to that of the SFBA fault system. The two very long parallel strike-slip faults, separated by distance $d = 20$, are subdivided into four fault segments A–D (Figure 7). Fault segment A extends from $-d/2$ on the x axis to infinity in both the $+y$ and $-y$ directions, slipping continuously below some depth L_d. Parallel to fault A, fault B extends from $+d/2$ on the x axis to infinity in the $+y$ direction, and fault C also begins at $+d/2$ on the x axis but extends to infinity in the $-y$ direction. Both B and C slip continuously below L_d. When faults B and C slip at the same rate, this is identical to a single throughgoing vertical strike slip fault, and the model is kinematically consistent. This model configuration allows us to introduce a slip rate discontinuity by changing the slip rate on fault B, creating a kinematically inconsistent set of fault slip rates. We

additionally include fault D as a 20 km long mesh of 312 triangular dislocation elements between the locking depth and the surface above fault A, centered at $y = 0$. We assume fault D is fully locked.

[19] We define a set of synthetic observation points on the free surface of the elastic halfspace, and calculate synthetic velocities from a forward model with prescribed slip rates. These synthetic velocities are inverted for estimates of slip rates on the deep dislocations and spatially variable creep on fault D. In contrast to the block model in which we directly estimate slip deficit rates, this simple model is constructed in the deep dislocation framework, and we directly estimate creep rates on fault D. We generate synthetic observation velocities assuming a fully locked upper crust, therefore nonzero slip estimated on fault D will be a model artifact, allowing us to evaluate the influence of kinematic inconsistency on creep distributions resolved on nearby faults.

[20] To demonstrate the differences between kinematically consistent and inconsistent models of kinematically consistent deformation, we generate synthetic velocities computed from a kinematically consistent forward model (Figure 8) such that the slip rates on faults A, B, and C are all equal to 10 mm/yr. We then invert these velocities within their original framework for slip on the faults and on the triangular dislocations. In this case of retaining kinematic consistency within the inversion, we recover 10 mm/yr slip rates on faults A, B, and C, and resolve negligible artificial slip on the triangular dislocation elements (Figure 8a). To understand the effects of kinematically consistent models, we invert these velocities for fault slip a second time, assigning a priori slip rate constraints of 10 mm/yr on faults A and C and 5 mm/yr on fault B. Kinematic inconsistency arises because a path integral of slip across the positive half of the fault system now differs from the path integral of slip across the negative half of the fault system. The residual velocity field now contains edge effects due to the jump in slip rate along strike (Figure 8b), and mesh of triangular dislocation elements is the only source of additional surface deformation available to accommodate the difference between the kinematically consistent forward field and the imposed deep slip rates. In this case, kinematic inconsistency within the model creates artifacts that map into a near-surface creep distribution on fault D (Figure 8b). The magnitude and spatial distribution of artificial slip depend on the smoothing parameters and geometry of the fault system. In the synthetic case shown in Figure 8b, this results in a maximum right lateral creep rate of 28 mm/yr and a maximum left lateral creep rate of 11 mm/yr.

[21] Although mapped fault traces are finite, traveling from stable North America to the Pacific plate without accommodating the geodetically [*Argus and Gordon*, 1990; *Argus and Heflin*, 1995] or geologically [*DeMets et al.*, 1994] observed total tectonic deformation would imply path dependence to relative plate tectonic motions. Maintaining kinematic consistency within a plate boundary model therefore requires the assumption of fault system continuity, in which continuous structures may represent deformation accommodated by diffuse deformation or poorly exposed faults.

[22] As an example, consider Figure 8c, in which 10 mm/yr of right-lateral slip is distributed over eleven parallel faults (1/6th km spacing), representing a case where deformation is more distributed. Even though deformation
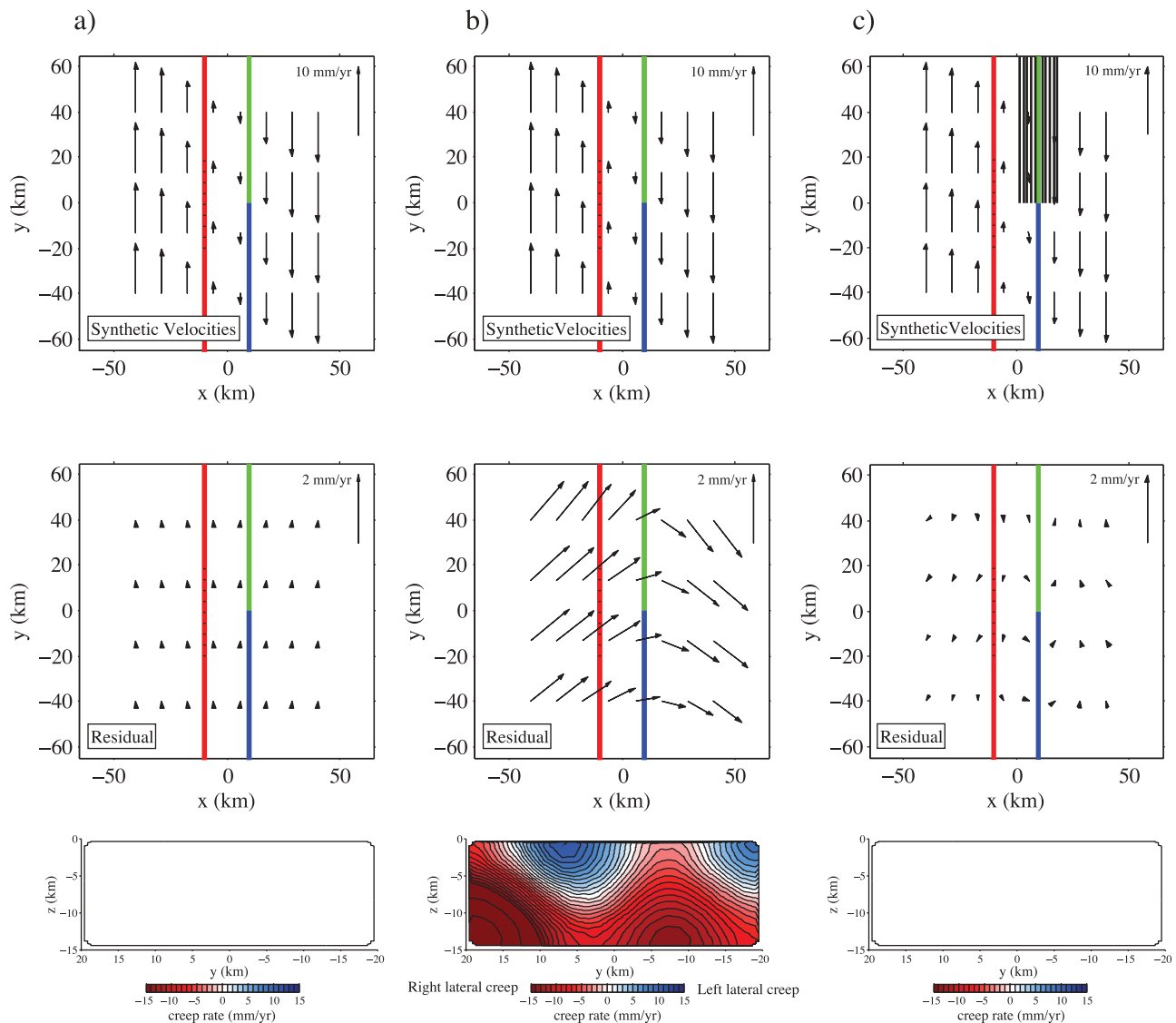
Figure 8. (a) Kinematically consistent synthetic velocities generated by a forward model with slip rates of 10 mm/yr on faults A, B, and C. When synthetic velocities are inverted assuming kinematic consistency, no modeling artifacts map onto the mesh of triangular dislocations. (b) Kinematically consistent synthetic velocities generated with slip rates of 10 mm/yr on faults A, B, and C. When forward velocities are inverted assuming an a priori slip rate of 5 mm/yr imposed on fault C (green), this produces artificial slip on the triangular dislocations. (c) In this forward model, 10 mm/yr of right lateral slip near fault C is distributed over 11 parallel faults. Faults A and B slip at 10 mm/yr. Approximating diffuse slip with a single fault C produces negligible modeling artifacts.

is distributed, the model is kinematically consistent because the total amount of slip does not vary across the system. As before, solving for creep on fault D recovers zero creep. We then model the same synthetic velocities with a slightly different model geometry, where the 11 parallel faults are represented as a single fault slipping at 10 mm/yr. Because the simplified geometry maintains kinematic consistency, inverting velocities predicted by the diffuse deformation model with this simplified single fault geometry produces negligible modeling artifacts on the near surface creep distribution. At the scale of the simple model used here, creep rate estimates on fault D are weakly sensitive to the exact geometry at the junction of faults B and C, so long as the

slip budget is kinematically consistent. Based on these simple models, it is possible that differences between our reference creep estimate and previous creep estimates [*Schmidt et al.*, 2005; Funning et al., submitted manuscript, 2011] may result from different assumptions about the kinematic consistency of the SFBA fault system.

7. Discussion

[23] We find that geodetically constrained slip rate estimates from our reference block model agree, within reported uncertainties, with geologic slip rate estimates along 6 of 10 SFBA faults (Figure 4). Our slip rate estimate on the Hayward fault of 6.7 ± 0.8 mm/yr is 1 to 4 mm/yr lower than

previous geologic and geodetic estimates [*d'Alessio et al.*, 2005; *Schmidt et al.*, 2005, *Simpson et al.*, 2001]. Because the Hayward fault may merge with, and transfer slip from, the Calaveras fault at its southern end, the geologic slip rate of 8 ± 2 mm/yr estimated by *Lienkaemper and Borchardt* [1996] at Union City, California, may not be representative of slip rate on the northern portion of the Hayward fault. Slip rates on the Calaveras and Greenville faults are slightly faster (~40% and ~100% respectively) than geologic estimates [*Kelson et al.*, 1996; *Berger et al.*, 2010], suggesting that structures east of the Hayward fault may currently accommodate more than twice the slip of the Hayward fault itself. In particular, because the estimated interseismic slip rate of 9.0 ± 0.9 mm/yr on the partially creeping Calaveras fault [*Manaker et al.*, 2003] exceeds that of the Hayward fault by 40%, the Calaveras fault may be capable of producing earthquakes that are larger or more frequent than those on the Hayward fault.

[24] We estimate the long-term fault slip rate on the Hayward fault to be 6.7 ± 0.8 mm/yr, and find maximum slip deficit rates of 4.2 ± 1.4 mm/yr at depth beneath Point Pinole, although data density severely limits resolution in this region. Between San Leandro and Fremont, slip deficit rates reach up to 3.7 ± 1.2 mm/yr at the surface. This 20 km region of high slip deficit rate is consistent in length and location with the observed surface rupture in the 1868 Hayward fault earthquake [*Lawson*, 1908]. Over 150 years, temporally invariant behavior of this patch would produce moment accumulation equivalent to a $M_W \approx 6.6$ earthquake, estimated with an empirical area-slip scaling relationship [*Wells and Coppersmith*, 1994]. Although deep features are poorly resolved, a fully locked patch on the Hayward fault at depth is not required to accumulate sufficient moment to generate a major earthquake over Hayward fault recurrence intervals of 161 ± 65 years [*Lienkaemper et al.*, 2010]. The pattern and magnitude of fault creep in the reference model are most consistent with the shallow creep distribution of *Bürgmann et al.* [2000], in which SFBA faults are represented as kinematically consistent deep dislocations.

[25] A correlation between geodetically imaged interseismic fault coupling and historical earthquake rupture location may be interpreted as consistent with the hypothesis of characteristic fault behavior [*Shimazaki and Nakata*, 1980; *Schwartz and Coppersmith*, 1984] and persistent seismic asperities [*Lay and Kanamori*, 1980]. In this idealized view, episodic earthquakes of similar magnitude occur at a characteristic location, and the ruptured portion of the fault remains locked during the interseismic period. Although the characteristic earthquake concept may oversimplify fault behavior, studies of interseismic coupling in subduction zones off Japan [*Yamanaka and Kikuchi*, 2004; *Nishimura et al.*, 2004; *Loveless and Meade*, 2010], Sumatra [*Konca et al.*, 2008], South America [*Moreno et al.*, 2010], and Alaska [*Cross and Freymueller*, 2007; *Suito and Freymueller*, 2009] also suggest that fault patches that are strongly coupled during the interseismic period are colocated with the hypocenters or rupture areas of large earthquakes.

[26] On the other hand, there is also evidence that creeping regions may not be temporally invariant. Coral records offshore off Sumatra suggest time and space variable patterns of strain accumulation over multiple earthquake cycles [*Natawidjaja et al.*, 2004], and coupled asperities at the New Britain trench off the coast of Papua New Guinea suggest that interseismically locked regions may not have controlled the locations of historic earthquakes [*Park and Mori*, 2007]. Another possibility is that the 1868 earthquake was able to rupture through a region of low coseismic slip deficit rather than be confined to the most strongly coupled patches [e.g., *Malservisi et al.*, 2003; *Malservisi et al.*, 2005]. Large historical events have also occurred along the Japan trench [*Nishimura et al.*, 2004] and offshore Sumatra [*Konca et al.*, 2008], in regions of low estimated coupling. Numerical models show that earthquake rupture on a fault with heterogenous frictional properties may not be confined to a velocity weakening patch imbedded within an otherwise velocity strengthening fault [*Kaneko and Lapusta*, 2008]. Similar models show that earthquakes may rupture through weakly coupled regions between separate highly coupled asperities [*Kaneko et al.*, 2010] and the nature of the earthquake rupture may not be consistent over multiple earthquake cycles, consistent with interpretation of seismic observations [e.g., *Thatcher*, 1990; *Freymueller et al.*, 2008]. Thus, low slip deficit rates surrounding a 20 km asperity on the Hayward fault may not preclude a longer 1868-type rupture extending from Berkeley to south of Fremont [e.g., *Yu and Segall*, 1996].

[27] Partially creeping behavior on the Hayward fault may be associated with complex lithologically modulated variations in frictional behavior of the rocks on either side of the Hayward fault. The region of partial creep we observe between San Leandro and Fremont is spatially coincident with a 25 km long gabbro body on the east face of the Hayward fault [*Graymer et al.*, 2005] (Figure 9). The adjacent west face consists of gabbro above 6 km depth and metagreywacke below. Although resolution of spatially variable creep is poor at depth, we image maximum slip deficit rates within this asperity near the surface. The collocation of a strongly coupled, though still creeping zone, with proximal gabbro units is notable given the apparent prevalence of this kinematic behavior in subduction zones where gabbro is regularly present [*Liu and Rice*, 2009]. Experiments to determine the frictional properties of gabbro at low temperatures and pressures reveal a complex range of behaviors. *Morrow and Lockner* [2001] performed failure and frictional sliding tests on rock samples collected at in situ along the Hayward fault and found that all of the samples, consisting of gabbro, coarse gabbro, keratophyre, altered keratophyre, basalt, sandstone and serpentinite, exhibit velocity strengthening behavior at temperature and pressures of 30–200 MPa. At an effective pressure of 30 MPa, the coarse gabbro is the least velocity strengthening of Hayward fault rocks. A similar set of experiments by *Marone and Cox* [1994] show that the velocity dependence of gabbro depends on contact roughness and total fault displacement, such that under 5 MPa normal stress at ambient temperatures, a smooth gabbro surface exhibits velocity weakening behavior while rough gabbro is velocity strengthening at slip distances less than 50 mm. At near surface temperatures and pressures, most rocks have been found to be velocity strengthening enabling interseismic creep, with creep rate magnitude a function of the frictional parameters, stress history, and boundary conditions [*Marone*, 1998]. Frictional experiments on dry gabbro have suggested that the transition from velocity strengthening to velocity
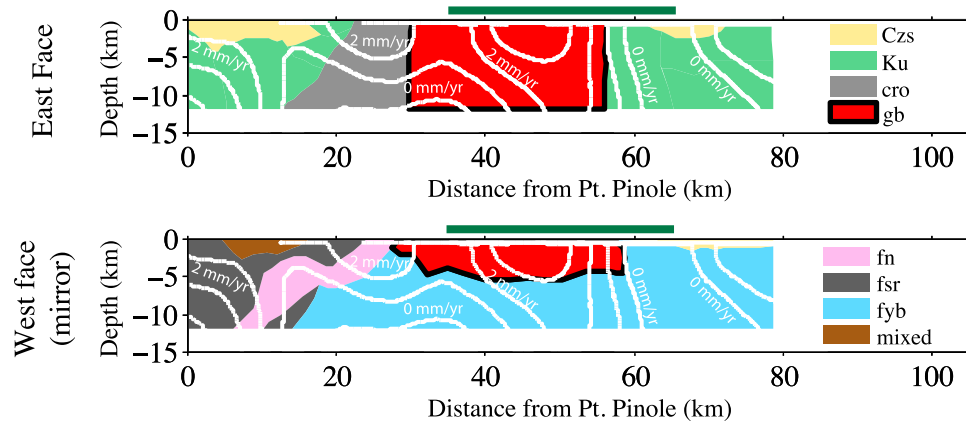
Figure 9. Fault surface geology reproduced from *Graymer et al.* [2005] with coupling rate contours. Jurassic gabbro (gb) shown in red. (top) Eastern face of the Hayward fault. (bottom) Western face (mirror image) of the Hayward fault. The green bar represents the observed surface trace of the 1868 Hayward earthquake. Rock types are Czs, Cenozoic sedimentary rocks; Ku, Upper Cretaceous sandstone, shale, and minor conglomerate; cro, undivided Jurassic serpentinite, gabbro, basalt, and keratophyre, with minor sedimentary rocks; gb, Jurassic gabbro; fn, Upper Cretaceous sandstone and shale; fsr: melange; fyb, Cretaceous metagreywacke; mixed, tectonically interleaved sandstone, metasandstone, melange, and serpentinite [*Graymer et al.*, 2005].

weakening occurs at temperatures between 250 and 510 degrees at atmospheric pressures [*He et al.*, 2007]. Assuming pressure effects on frictional parameters are negligible, these experiments would suggest that a transition between velocity weakening and velocity strengthening occurs near a depth of 8.3 km assuming a regional geothermal gradient of 30°C/km. While current geodetic data are insufficient to provide kilometer-scale resolution downdip, experimental results are consistent with geodetically constrained estimates of a creep transition midway through the upper crust.

8. Conclusion

[28] To better constrain the kinematic parameters necessary for quantitative seismic hazard assessment and understand the interseismic behavior of the Hayward fault, we invert GPS and InSAR data with a kinematically consistent block model of the SFBA fault system to estimate Bay Area fault slip rates and spatially variable slip deficit rates on the Hayward fault. Checkerboard resolution tests on the Hayward fault reveal that slip deficit features <15 km long are well resolved along strike at the surface, but cannot be robustly resolved deeper than 7 km with published GPS and InSAR data. Simple models of a two-fault system suggest that, at scales comparable to that of the SFBA fault system, estimated creep rates at depth are sensitive to assumptions about the kinematic consistency of slip rates on neighboring faults, and may contribute to differences between this and previous estimates of creep rates at depth on the Hayward fault. We identify a strongly coupled asperity with a slip deficit rate of 3.7 ± 1.2 mm/yr at the surface near San Leandro, California. Spatial correlation between high slip deficit rates and gabbroic fault surfaces adjacent to the mapped surface trace of the 1868 M_W = 6.9–7.0 suggests that partially creeping fault behavior may be associated with complex lithologically modulated variations in frictional properties. Further insight into whether or not geodetically imaged asperities limit the rupture extent of future

earthquakes on the Hayward fault may be gained through dynamic slip models that are evolved forward in time from present-day conditions.

Appendix A: Block Modeling With Spatially Variable Fault Coupling and InSAR Observations

[29] The linear block model formulation, explicitly stated for GPS velocities in terms of linear operators by *Meade and Loveless* [2009], interprets interseismic geodetic velocities, v_I, as resulting from a combination of microplate or block rotations, v_B, quasistatic earthquake cycle processes, v_E, and residual velocities, v_r:

$$v_I = v_B + v_E + v_r. \qquad (A1)$$

[30] A homogeneous internal strain rate may also be included in the velocity field decomposition, but since we do not estimate internal strain in this study, we do not include it here.

[31] The discussion that follows extends, and requires, the mathematical framework detailed previously by *Meade and Loveless* [2009]. Velocities due to elastic earthquake cycle processes are modeled assuming that all faults are fully coupled between the surface and an inferred locking depth using rectangular dislocations [*Okada*, 1985] in a homogeneous elastic half-space [e.g., *Savage*, 1983; *Matsu'ura et al.*, 1986]. We describe these velocities, v_{CSD}, as resulting from interseismic elastic strain accumulation across a locked fault, represented by removing the coseismic slip deficit from the static block offset. Where geodetic data are sufficiently dense and/or where rectangular elements inadequately describe fault geometry, we incorporate a continuous mesh of triangular dislocation elements to allow coupling rate estimates on a smoothly interpolated three-dimensional fault surface. We simultaneously estimate elastic coseismic slip deficit on each of these triangular dislocation elements [*Comninou*, 1973; *Jeyakumaran et al.*, 1992; *Thomas*, 1993; *Meade*, 2007]. Incorporating v_{CSD} and the velocities due

to slip on triangular dislocation elements, v_{TDE}, into equation (A1) outlines the linear forward problem [*Meade and Loveless*, 2009].

$$v_I = v_B - (v_{CSD} + v_{TDE}) + v_r \qquad (A2)$$

[32] We expand the formulation here to include InSAR line-of-sight measurements. Unlike GPS east-north-up velocities, InSAR data record one component of interseismic velocity, $\widehat{v}_I$, in the satellite look direction. For the satellite data included in this study, the look vector has east, north, and up components given by $l = [0.389 - 0.078 \ 0.918]$. To account for orbital baseline unknowns in the InSAR measurements, we simultaneously solve for a best fitting quadratic ramp from the data. We choose a quadratic ramp because InSAR orbital errors are approximately quadratic in space [*Zebker et al.*, 1994]. The solution does not change significantly with a linear ramp. We decompose the line-of-sight velocities as in equation (A2), considering the line-of-sight velocities, $\widehat{v}_q$, due to the additional ramp parameter:

$$\widehat{v}_I = \widehat{v}_B - (\widehat{v}_{CSD} + \widehat{v}_{TDE}) + \widehat{v}_r + \widehat{v}_q. \qquad (A3)$$

[33] The velocity components defined in equation (A3) are related to the estimated block model parameters using the linear operators defined by *Meade and Loveless* [2009], with the addition of the linear operator P_L, which converts east-north-up velocities to a line-of-sight range change rate to ENU velocities based on the look vector l.

$$P_L = \begin{bmatrix} l_e & l_n & l_u & & 0 & 0 & 0 \\ & & & \ddots & & & \\ 0 & 0 & 0 & & l_e & l_n & l_u \end{bmatrix} \qquad (A4)$$

[34] For each component of the velocity field decomposition, InSAR LOS velocities must be converted from XYZ velocities to east-north-up velocities, and reduced to a line-of-site range change rate by premultiplying terms from *Meade and Loveless* [2009] by P_L. For example, the block rotation rate is explicitly written as

$$\widehat{v}_B = P_L P_{V_s} G_{B_s} \Omega, \qquad (A5)$$

in which P_{V_s} is a geometric transformation that converts XYZ rotation velocities at InSAR observation locations into east-north-up velocities; G_{B_s} is the generalized matrix of partial derivatives for each InSAR observation point with respect to the rotation vector, and Ω contains the elements of a Cartesian rotation vector.

[35] Finally we estimate a quadratic ramp to account for uncertainties in the orbital parameters assumed in InSAR processing. These uncertainties can map into the derived velocity field as a quadratic form varying in latitude and longitude [*Zebker et al.*, 1994]. Because the line-of-sight contribution of the quadratic ramp is calculated in the look direction, we do not have to convert the ramp parameters to east-north-up:

$$\widehat{v}_q = G_q q \qquad (A6)$$

G_q contains 6 columns for every InSAR line-of-sight observation for each coefficient in the quadratic ramp, and q is a 6-by-1 array containing the ramp coefficients.

[36] In order to estimate block model parameters, we use a weighted least squares inversion to simultaneously estimate block rotations, Ω^{est}, smoothed coupling on triangular dislocation elements, t^{est}:

$$\begin{bmatrix} \Omega^{est} \\ t^{est} \\ q \end{bmatrix} = (G^T W G)^{-1} G^T W \begin{bmatrix} \widetilde{v}_{GPS} \\ \widehat{v}_{SAR} \\ s_{obs} \\ 0 \\ t_{bc} \end{bmatrix}, \qquad (A7)$$

in which G is the generalized combined Jacobian relating the estimated parameters to GPS velocities, $\widetilde{v}_{GPS}$, InSAR range change rates, $\widehat{v}_{SAR}$, and a priori slip rate observations, s_{obs}. We additionally impose smoothing constraints on the mesh of triangular dislocation elements by minimizing the gradient of the slip distribution. We select a smoothing value that maintains realistic coupling values. The vector t_{bc} defines the boundary conditions on the mesh of triangular dislocation elements. Relative data weights are determined by the weighting matrix W:

$$W = \begin{bmatrix} C_{GPS}^{-1} & 0 & 0 & 0 & 0 \\ 0 & \beta_{SAR} C_{SAR}^{-1} & 0 & 0 & 0 \\ 0 & 0 & \beta_{ap} C_{obs}^{-1} & 0 & 0 \\ 0 & 0 & 0 & \beta^* I & 0 \\ 0 & 0 & 0 & 0 & \beta_{bc} C_{bc}^{-1} \end{bmatrix} \qquad (A8)$$

in which C_{GPS}^{-1}, C_{SAR}^{-1}, C_{obs}^{-1}, and C_{bc}^{-1} are the GPS, SAR, a priori observation, and boundary condition covariance matrices, respectively. Weights of each data set relative to GPS velocities are given by constants β_{SAR} β_{ap}, β^*, and β_{bc}. I is the identity matrix associated with the smoothing constraint.

References

Argus, D. F., and R. G. Gordon (1990), Pacific North-American plate motion from very long base-line interferometry compared with motion inferred from magnetic anomalies, transform faults, and earthquake slip vectors, *J. Geophys. Res.*, *95*(B11), 17,315–17,324, doi:10.1029/JB095iB11p17315.

Argus, D. F., and R. G. Gordon (2001), Present tectonic motion across the Coast Ranges and San Andreas fault system in central California, *Geol. Soc. Am. Bull.*, *113*(12), 1580–1592, doi:10.1130/0016-7606(2001) 113<1580:PTMATC>2.0.CO;2.

Argus, D. F., and M. B. Heflin (1995), Plate motion and crustal deformation estimated with geodetic data from the global positioning system, *Geophys. Res. Lett.*, *22*(15), 1973–1976, doi:10.1029/95GL02006.

Bakun, W. H. (1999), Seismic activity of the San Francisco Bay region, *Bull. Seismol. Soc. Am.*, *89*(3), 764–784.

Becker, T. W., J. L. Hardebeck, and G. Anderson (2005), Constraints on fault slip rates of the southern California plate boundary from GPS velocity and stress inversions, *Geophys. J. Int.*, *160*(2), 634–650, doi:10.1111/j.1365-246X.2004.02528.x.

Bennett, R. A., W. Rodi, and R. E. Reilinger (1996), Global positioning system constraints on fault slip rates in southern California and northern Baja, Mexico, *J. Geophys. Res.*, *101*(B10), 21,943–21,960, doi:10.1029/96JB02488.

Berger, G. W., T. L. Sawyer, and J. R. Unruh (2010), Single- and multigrain luminescence dating of sediments related to the Greenville fault, eastern San Francisco Bay Area, California, *Bull. Seismol. Soc. Am.*, *100*(3), 1051–1072, doi:10.1785/0120090310.

Bilham, R., and S. Whitehead (1997), Subsurface creep on the Hayward fault, Fremont, California, *Geophys. Res. Lett.*, *24*(11), 1307–1310, doi:10.1029/97GL01244.

Borchardt, G. S., L. David, and C. J. Wills (1999), Holocene slip rate of the Concord fault at Galindo Creek in Concord, California: National Earthquake Hazards Program final technical report, U. S. Geol. Surv. Libr., Reston, Va.

Budding, K. E., D. P. Schwartz, and D. H. Oppenheimer (1991), Slip rate, earthquake recurrence, and seismogenic potential of the Rodgers Creek fault zone, northern California: Initial results, *Geophys. Res. Lett.*, *18*, 447–450, doi:10.1029/91GL00465.

Bürgmann, R., P. Segall, M. Lisowski, and J. Svarc (1997), Postseismic strain following the 1989 Loma Prieta earthquake from GPS and leveling measurements, *J. Geophys. Res.*, *102*(B3), 4933–4955, doi:10.1029/96JB03171.

Bürgmann, R., D. Schmidt, R. M. Nadeau, M. d'Alessio, E. Fielding, D. Manaker, T. V. McEvilly, and M. H. Murray (2000), Earthquake potential along the northern Hayward fault, California, *Science*, *289*(5482), 1178–1182, doi:10.1126/science.289.5482.1178.

Bürgmann, R., M. G. Kogan, G. M. Steblov, G. Hilley, V. E. Levin, and E. Apel (2005), Interseismic coupling and asperity distribution along the Kamchatka subduction zone, *J. Geophys. Res.*, *110*, B07405, doi:10.1029/2005JB003648.

Bürgmann, R., G. Hilley, A. Ferretti, and F. Novali (2006), Resolving vertical tectonics in the San Francisco Bay Area from permanent scatterer InSAR and GPS analysis, *Geology*, *34*(3), 221–224, doi:10.1130/G22064.1.

Comninou, M. (1973), Angular dislocation in a half space, PhD dissertation, 45 pp., Northwestern Univ., Evanston, Ill.

Cross, R. S., and J. T. Freymueller (2007), Plate coupling variation and block translation in the Andreanof segment of the Aleutian arc determined by subduction zone modeling using GPS data, *Geophys. Res. Lett.*, *34*, L06304, doi:10.1029/2006GL028970.

d'Alessio, M. A., I. A. Johanson, R. Bürgmann, D. A. Schmidt, and M. H. Murray (2005), Slicing up the San Francisco Bay Area: Block kinematics and fault slip rates from GPS-derived surface velocities, *J. Geophys. Res.*, *110*, B06403, doi:10.1029/2004JB003496.

DeMets, C., R. G. Gordon, D. F. Argus, and S. Stein (1994), Effect of recent revisions to the geomagnetic reversal time-scale on estimates of current plate motions, *Geophys. Res. Lett.*, *21*(20), 2191–2194, doi:10.1029/94GL02118.

Freymueller, J. T., M. H. Murray, P. Segall, and D. Castillo (1999), Kinematics of the Pacific–North America plate boundary zone, northern California, *J. Geophys. Res.*, *104*(B4), 7419–7441, doi:10.1029/1998JB900118.

Freymueller, J. T., H. Woodard, S. Cohen, R. Cross, J. Elliott, C. Larsen, S. Hreinsdottir, and C. Zweck (2008), Active deformation processes in Alaska, based on 15 years of GPS measurements, in *Active Tectonics and Seismic Potential of Alaska*, *AGU Geophys. Monogr. Ser.*, vol. 179, edited by J. T. Freymueller et al., pp. 1–42, AGU, Washington, D. C., doi:10.1029/179GM02.

Graymer, R. W., A. M. Sarna-Wojcicki, J. P. Walker, R. J. McLaughlin, and R. J. Fleck (2002), Controls on timing and amount of right-lateral offset on the East Bay fault system, San Francisco Bay region, California, *Geol. Soc. Am. Bull.*, *114*(12), 1471–1479, doi:10.1130/0016-7606(2002)114<1471:COTAAO>2.0.CO;2.

Graymer, R. W., D. A. Ponce, R. C. Jachens, R. W. Simpson, G. A. Phelps, and C. M. Wentworth (2005), Three-dimensional geologic map of the Hayward fault, northern California: Correlation of rock units with variations in seismicity, creep rate, and fault dip, *Geology*, *33*(6), 521–524, doi:10.1130/G21435.1.

Hall, N. T., R. H. Wright, and K. B. Clahan (1999), Paleoseismic studies of the San Francisco peninsula segment of the San Andreas fault zone near Woodside, California, *J. Geophys. Res.*, *104*(B10), 23,215–23,236, doi:10.1029/1999JB900157.

Hardebeck, J. L., A. J. Michael, and T. M. Brocher (2007), Seismic velocity structure and seismotectonics of the eastern San Francisco Bay region, California, *Bull. Seismol. Soc. Am.*, *97*(3), 826–842, doi:10.1785/0120060032.

Harris, R. A., and P. Segall (1987), Detection of a locked zone at depth on the Parkfield, California, segment of the San Andreas fault, *J. Geophys. Res.*, *92*(B8), 7945–7962, doi:10.1029/JB092iB08p07945.

He, C. R., Z. L. Wang, and W. M. Yao (2007), Frictional sliding of gabbro gouge under hydrothermal conditions, *Tectonophysics*, *445*(3–4), 353–362, doi:10.1016/j.tecto.2007.09.008.

Humphreys, E. D., and R. J. Weldon (1994), Deformation across the western United States: A local estimate of Pacific–North America transform deformation, *J. Geophys. Res.*, *99*(B10), 19,975–20,010, doi:10.1029/94JB00899.

Jeyakumaran, M., J. W. Rudnicki, and L. M. Keer (1992), Modeling slip zones with triangular dislocation elements, *Bull. Seismol. Soc. Am.*, *82*, 2153–2169.

Johanson, I. A., and R. Bürgmann (2005), Creep and quakes on the northern transition zone of the San Andreas fault from GPS and InSAR data, *Geophys. Res. Lett.*, *32*, L14306, doi:10.1029/2005GL023150.

Johnson, K. M., and J. Fukuda (2010), New methods for estimating the spatial distribution of locked asperities and stress-driven interseismic creep on faults with application to the San Francisco Bay region, California, *J. Geophys. Res.*, *115*, B12408, doi:10.1029/2010JB007703.

Kaneko, Y., and N. Lapusta (2008), Variability of earthquake nucleation in continuum models of rate-and-state faults and implications for aftershock rates, *J. Geophys. Res.*, *113*, B12312, doi:10.1029/2007JB005154.

Kaneko, Y., J.-P. Avouac, and N. Lapusta (2010), Towards inferring earthquake patterns from geodetic observations of interseismic coupling, *Nat. Geosci.*, *3*(5), 363–369, doi:10.1038/ngeo843.

Kelson, K. I., G. D. Simpson, W. R. Lettis, and C. C. Haraden (1996), Holocene slip rate and recurrence of the northern Calaveras fault at Leyden Creek, eastern San Francisco Bay region, *J. Geophys. Res.*, *101*(B3), 5961–5975, doi:10.1029/95JB02244.

Konca, A. O., et al. (2008), Partial rupture of a locked patch of the Sumatra megathrust during the 2007 earthquake sequence, *Nature*, *456*(7222), 631–635, doi:10.1038/nature07572.

Lawson, A. C. (Ed.) (1908), *The California Earthquake of April 18, 1906, Report of the State Earthquake Investigation Commission*, vol. 1, Carnegie Inst. of Wash., Washington, D. C.

Lay, T., and H. Kanamori (1980), Earthquake doublets in the Solomon Islands, *Phys. Earth Planet. Inter.*, *21*(4), 283–304, doi:10.1016/0031-9201(80)90134-X.

Lienkaemper, J. J., and G. Borchardt (1996), Holocene slip rate of the Hayward fault at Union City, California, *J. Geophys. Res.*, *101*(B3), 6099–6108, doi:10.1029/95JB01378.

Lienkaemper, J. J., and J. S. Galehouse (1998), New evidence doubles the seismic potential of the Hayward fault, *Seismol. Res. Lett.*, *69*(6), 519–523, doi:10.1785/gssrl.69.6.519.

Lienkaemper, J. J., J. S. Galehouse, and R. W. Simpson (1997), Creep response of the Hayward fault to stress changes caused by the Loma Prieta earthquake, *Science*, *276*(5321), 2014–2016, doi:10.1126/science.276.5321.2014.

Lienkaemper, J. J., J. S. Galehouse, and R. W. Simpson (2001), Long-term monitoring of creep rate along the Hayward fault and evidence for a lasting creep response to 1989 Loma Prieta earthquake, *Geophys. Res. Lett.*, *28*(11), 2265–2268, doi:10.1029/2000GL012776.

Lienkaemper, J. J., P. L. Williams, and T. P. Guilderson (2010), Evidence for a 12th large earthquake on the southern Hayward fault in the past 1900 years, *Bull. Seismol. Soc. Am.*, *100*, 2024–2034.

Liu, Y. J., and J. R. Rice (2009), Slow slip predictions based on granite and gabbro friction data compared to GPS measurements in northern Cascadia, *J. Geophys. Res.*, *114*, B09407, doi:10.1029/2008JB006142.

Loveless, J. P., and B. J. Meade (2010), Geodetic imaging of plate motions, slip rates, and partitioning of deformation in Japan, *J. Geophys. Res.*, *115*, B02410, doi:10.1029/2008JB006248.

Maerten, F., P. Resor, D. Pollard, and L. Maerten (2005), Inverting for slip on three-dimensional fault surfaces using angular dislocations, *Bull. Seismol. Soc. Am.*, *95*(5), 1654–1665, doi:10.1785/0120030181.

Malservisi, R., C. Gans, and K. P. Furlong (2003), Numerical modeling of strike-slip creeping faults and implications for the Hayward fault, California, *Tectonophysics*, *361*(1–2), 121–137, doi:10.1016/S0040-1951(02)00587-5.

Malservisi, R., K. P. Furlong, and C. R. Gans (2005), Microseismicity and creeping faults: Hints from modeling the Hayward fault, California (USA), *Earth Planet. Sci. Lett.*, *234*, 421–435, doi:10.1016/j.epsl.2005.02.039.

Manaker, D. M., R. Bürgmann, W. H. Prescott, and J. Langbein (2003), Distribution of interseismic slip rates and the potential for significant earthquakes on the Calaveras fault, central California, *J. Geophys. Res.*, *108*(B6), 2287, doi:10.1029/2002JB001749.

Manaker, D. M., A. J. Michael, and R. Bürgmann (2005), Subsurface structure and kinematics of the Calaveras-Hayward fault stepover from three-dimensional V_p and seismicity, San Francisco Bay region, California, *Bull. Seismol. Soc. Am.*, *95*(2), 446–470, doi:10.1785/0120020202.

Marone, C. (1998), Laboratory-derived friction laws and their application to seismic faulting, *Annu. Rev. Earth Planet. Sci.*, *26*, 643–696, doi:10.1146/annurev.earth.26.1.643.

Marone, C., and S. J. D. Cox (1994), Scaling of rock friction constitutive parameters: The effects of surface roughness and cumulative offset on friction of gabbro, *Pure Appl. Geophys.*, *143*(1–3), 359–385, doi:10.1007/BF00874335.

Matsu'ura, M., D. D. Jackson, and A. Cheng (1986), Dislocation model for aseismic crustal deformation at Hollister, California, *J. Geophys. Res.*, *91*(B12), 2661–2674.

McCaffrey, R. (2002), Crustal block rotations and plate coupling, in *Plate Boundary Zones*, *Geodyn. Ser.*, vol. 30, edited by S. Stein and J. Freymueller, pp. 101–122, AGU, Washington, D. C., doi:10.1029/GD030p0101.

McCaffrey, R. (2009), Time-dependent inversion of three-component continuous GPS for steady and transient sources in northern Cascadia, *Geophys. Res. Lett.*, *36*, L07304, doi:10.1029/2008GL036784.

Meade, B. J. (2007), Algorithms for the calculation of exact displacements, strains, and stresses for triangular dislocation elements in a uniform elastic half-space, *Comput. Geosci.*, *33*(8), 1064–1075, doi:10.1016/j.cageo.2006.12.003.

Meade, B. J., and B. H. Hager (2005), Block models of crustal motion in southern California constrained by GPS measurements, *J. Geophys. Res.*, *110*, B03403, doi:10.1029/2004JB003209.

Meade, B. J., and J. P. Loveless (2009), Block modeling with connected fault-network geometries and a linear elastic coupling estimator in spherical coordinates, *Bull. Seismol. Soc. Am.*, *99*(6), 3124–3139, doi:10.1785/0120090088.

Menke, W. (1984), *Geophysical Data Analysis: Discrete Inverse Theory*, Academic, San Diego, Calif.

Minster, J. B., and T. H. Jordan (1978), Present-day plate motions, *J. Geophys. Res.*, *83*(B11), 5331–5354, doi:10.1029/JB083iB11p05331.

Moreno, M., M. Rosenau, and O. Oncken (2010), 2010 Maule earthquake slip correlates with pre-seismic locking of Andean subduction zone, *Nature*, *467*(7312), 198–202, doi:10.1038/nature09349.

Morrow, C. A., and D. A. Lockner (2001), Hayward fault rocks: Porosity, density, and strength measurements, *U.S. Geol. Surv. Open File Rep.*, *01-421*, 28pp.

Murray, M. H., and P. Segall (2001), Modeling broadscale deformation in northern California and Nevada from plate motions and elastic strain accumulation, *Geophys. Res. Lett.*, *28*(22), 4315–4318, doi:10.1029/2001GL013373.

Murray-Moraleda, J. R., and R. W. Simpson (2009), Geodetically inferred coseismic and postseismic slip due to the *M* 5.4 31 October 2007 Alum Rock earthquake, *Bull. Seismol. Soc. Am.*, *99*(5), 2784–2800, doi:10.1785/0120090017.

Natawidjaja, D. H., K. Sieh, S. N. Ward, H. Cheng, R. L. Edwards, J. Galetzka, and B. W. Suwargadi (2004), Paleogeodetic records of seismic and aseismic subduction from central Sumatran microatolls, Indonesia, *J. Geophys. Res.*, *109*, B04306, doi:10.1029/2003JB002398.

Niemi, T. M., and N. T. Hall (1992), Late Holocene slip rate and recurrence of great earthquakes on the San Andreas fault in northern California, *Geology*, *20*(3), 195–198, doi:10.1130/0091-7613(1992)020<0195:LHSRAR>2.3.CO;2.

Nishimura, T., T. Hirasawa, S. Miyazaki, T. Sagiya, T. Tada, S. Miura, and K. Tanaka (2004), Temporal change of interplate coupling in northeastern Japan during 1995–2002 estimated from continuous GPS observations, *Geophys. J. Int.*, *157*(2), 901–916, doi:10.1111/j.1365-246X.2004.02159.x.

Okada, Y. (1985), Surface deformation due to shear and tensile faults in a half-space, *Bull. Seismol. Soc. Am.*, *75*(4), 1135–1154.

Park, S. C., and J. Mori (2007), Are asperity patterns persistent? Implication from large earthquakes in Papua New Guinea, *J. Geophys. Res.*, *112*, B03303, doi:10.1029/2006JB004481.

Ponce, D. A., R. W. Simpson, R. W. Graymer, and R. C. Jachens (2004), Gravity, magnetic, and high-precision relocated seismicity profiles suggest a connection between the Hayward and Calaveras faults, northern California, *Geochem. Geophys. Geosyst.*, *5*, Q07004, doi:10.1029/2003GC000684.

Pritchard, M. E., M. Simons, P. A. Rosen, S. Hensley, and F. H. Webb (2002), Co-seismic slip from the 1995 July 30 M_w = 8.1 Antofagasta, Chile, earthquake as constrained by InSAR and GPS observations, *Geophys. J. Int.*, *150*(2), 362–376, doi:10.1046/j.1365-246X.2002.01661.x.

Sammis, C. G., and J. R. Rice (2001), Repeating earthquakes as low-stress-drop events at a border between locked and creeping fault patches, *Bull. Seismol. Soc. Am.*, *91*(3), 532–537, doi:10.1785/0120000075.

Savage, J. C. (1983), A dislocation model of strain accumulation and release at a subduction zone, *J. Geophys. Res.*, *88*(B6), 4984–4996, doi:10.1029/JB088iB06p04984.

Savage, J. C., and M. Lisowski (1993), Inferred depth of creep on the Hayward fault, central California, *J. Geophys. Res.*, *98*(B1), 787–793, doi:10.1029/92JB01871.

Schmalzle, G., T. Dixon, R. Malservisi, and R. Govers (2006), Strain accumulation across the Carrizo segment of the San Andreas fault, California: Impact of laterally varying crustal properties, *J. Geophys. Res.*, *111*, B05403, doi:10.1029/2005JB003843.

Schmidt, D. A., R. Bürgmann, R. M. Nadeau, and M. d'Alessio (2005), Distribution of aseismic slip rate on the Hayward fault inferred from seismic and geodetic data, *J. Geophys. Res.*, *110*, B08406, doi:10.1029/2004JB003397.

Schwartz, D. P., and K. J. Coppersmith (1984), Fault behavior and characteristic earthquakes: Examples from the Wasatch and San Andreas fault zones, *J. Geophys. Res.*, *89*(B7), 5681–5698, doi:10.1029/JB089iB07p05681.

Segall, P. (2002), Integrating geologic and geodetic estimates of slip rate on the San Andreas fault system, *Int. Geol. Rev.*, *44*(1), 62–82, doi:10.2747/0020-6814.44.1.62.

Shimazaki, K., and T. Nakata (1980), Time-predictable recurrence model for large earthquakes, *Geophys. Res. Lett.*, *7*(4), 279–282, doi:10.1029/GL007i004p00279.

Simpson, G. D., S. C. Thompson, J. S. Noller, and W. R. Lettis (1998), The northern San Gregorio fault zone: Evidence for the timing of late Holocene earthquakes near Seal Cove, California, *Bull. Seismol. Soc. Am.*, *87*(5), 1158–1170.

Simpson, G. D., J. N. Baldwin, K. I. Kelson, and W. R. Lettis (1999), Late Holocene slip rate and earthquake history for the northern Calaveras fault at Welch Creek, eastern San Francisco Bay Area, California, *Bull. Seismol. Soc. Am.*, *89*(5), 1250–1263.

Simpson, R. W., J. J. Lienkaemper, and J. S. Galehouse (2001), Variations in creep rate along the Hayward fault, California, interpreted as changes in depth of creep, *Geophys. Res. Lett.*, *28*(11), 2269–2272, doi:10.1029/2001GL012979.

Souter, B. J. (1998), Comparisons of geologic models to GPS observations in southern California, PhD dissertation, Mass. Inst. of Technol., Cambridge.

Suito, H., and J. T. Freymueller (2009), A viscoelastic and afterslip post-seismic deformation model for the 1964 Alaska earthquake, *J. Geophys. Res.*, *114*, B11404, doi:10.1029/2008JB005954.

Templeton, D. C., R. M. Nadeau, and R. Bürgmann (2008), Behavior of repeating earthquake sequences in central California and the implications for subsurface fault creep, *Bull. Seismol. Soc. Am.*, *98*(1), 52–65, doi:10.1785/0120070026.

Thatcher, W. (1990), Order and diversity in the modes of circum-Pacific earthquake recurrence, *J. Geophys. Res.*, *95*(B3), 2609–2623, doi:10.1029/JB095iB03p02609.

Thomas, A. (1993), POLY3D: A three-dimensional, polygonal element, displacement discontinuity boundary element computer program with applications to fractures, faults, and cavities in the Earth's crust, MS thesis, 69 pp., Stanford Univ., Palo Alto, Calif.

Toppozada, T., and D. Branum (2004), California earthquake history, *Ann. Geophys.*, *47*(2–3), 509–522.

2007 Working Group on California Earthquake Probabilities (2008), The uniform California earthquake rupture forecast, version 2 (UCERF 2), *U.S. Geol. Surv. Open File Rep.*, *2007-1437*, 104 pp.

Waldhauser, F., and W. L. Ellsworth (2002), Fault structure and mechanics of the Hayward fault, California, from double-difference earthquake locations, *J. Geophys. Res.*, *107*(B3), 2054, doi:10.1029/2000JB000084.

Wallace, L. M., J. Beavan, R. McCaffrey, and D. Darby (2004), Subduction zone coupling and tectonic block rotations in the North Island, New Zealand, *J. Geophys. Res.*, *109*, B12406, doi:10.1029/2004JB003241.

Weber, G. E., and J. M. Nolan (1995), *Determination of Late Pleistocene-Holocene Slip Rates Along the San Gregorio Fault Zone, San Mateo County, California*, 52 pp., Associates, Watsonville, Calif.

Wells, D. L., and K. J. Coppersmith (1994), New empirical relationships among magnitude, rupture length, rupture width, rupture area, and surface displacement, *Bull. Seismol. Soc. Am.*, *84*(4), 974–1002.

Williams, R. A., R. W. Simpson, R. C. Jachens, W. J. Stephenson, J. K. Odum, and D. A. Ponce (2005), Seismic reflection evidence for a northeast-dipping Hayward fault near Fremont, California: Implications for seismic hazard, *Geophys. Res. Lett.*, *32*, L13301, doi:10.1029/2005GL023113.

Yamanaka, Y., and M. Kikuchi (2004), Asperity map along the subduction zone in northeastern Japan inferred from regional seismic data, *J. Geophys. Res.*, *109*, B07307, doi:10.1029/2003JB002683.

Yu, E., and P. Segall (1996), Slip in the 1868 Hayward earthquake from the analysis of historical triangulation data, *J. Geophys. Res.*, *101*(B7), 16,101–16,118, doi:10.1029/96JB00806.

Zebker, H. A., P. A. Rosen, R. M. Goldstein, A. Gabriel, and C. L. Werner (1994), On the derivation of coseismic displacement fields using differential radar interferometry: The Landers earthquake, *J. Geophys. Res.*, *99*(B10), 19,617–19,634, doi:10.1029/94JB01179.

E. L. Evans and B. J. Meade, Department of Earth and Planetary Sciences, Harvard University, 20 Oxford St., Cambridge, MA 02138, USA. (elevans@fas.harvard.edu)

J. P. Loveless, Department of Geosciences, Smith College, Northampton, MA 01063, USA.